

Structural Determination of Catalytically Active Subnanometer Iron Oxide Clusters

Qi Yang,^{†,¶} Xin-Pu Fu,^{‡,¶} Chun-Jiang Jia,^{*,‡} Chao Ma,^{*,§} Xu Wang,[†] Jie Zeng,[§] Rui Si,^{*,†} Ya-Wen Zhang,^{||} and Chun-Hua Yan^{||}

[†]Shanghai Synchrotron Radiation Facility, Shanghai Institute of Applied Physics, Chinese Academy of Sciences, Shanghai 201204, China

[‡]Key Laboratory for Colloid and Interface Chemistry, Key Laboratory of Special Aggregated Materials, School of Chemistry and Chemical Engineering, Shandong University, Jinan 250100, China

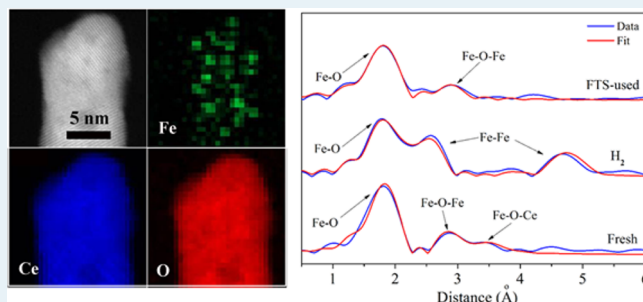
[§]Hefei National Laboratory for Physical Sciences at the Microscale, University of Science and Technology of China, Hefei, Anhui 230026, China

^{||}Beijing National Laboratory for Molecular Sciences, State Key Lab of Rare Earth Materials Chemistry and Applications, PKU-HKU Joint Lab in Rare Earth Materials and Bioinorganic Chemistry, Peking University, Beijing 100871, China

Supporting Information

ABSTRACT: Supported subnanometer clusters exhibit superiority in catalytic performance compared to common nanoparticles, due to their higher fraction of exposed surfaces and larger number of active species at the metal–support interface, responding to the size effect and the support effect in heterogeneous catalysis. Here, we report the synthesis of subnanometer iron oxide clusters anchored to the surfaces of two types of ceria nanoshapes (nanorods and nanopolyhedra), as well as the structure–activity relation investigation for Fischer–Tropsch synthesis. On the basis of the comprehensive structural characterizations including aberration-corrected scanning transmission electron microscopy (STEM) and X-ray absorption fine structure (XAFS), we demonstrated that the subnanometer clusters of iron oxide are stable and catalytically active for the Fischer–Tropsch synthesis reaction. Furthermore, it is identified that finely dispersed iron oxide clusters ($\text{Fe}-\text{O}_x-\text{Fe}_y$) consisted of partially reduced $\text{Fe}^{\delta+}$ ($\delta = 2.6-2.9$) species in ceria nanorods are active for Fischer–Tropsch synthesis; however, another type of iron oxide cluster ($\text{Fe}-\text{O}_x-\text{Ce}_y$) composed of fully oxidized Fe^{3+} ions strongly interacted with the ceria nanopolyhedra support but exhibits relatively poorer activity for the reaction. These results have broad implications on the fundamental understanding of active site of supported metal catalysts at the atomic level.

KEYWORDS: subnanometer cluster, iron–ceria, active site, metal–support interaction, structure–activity relationship



1. INTRODUCTION

To develop an efficient heterogeneous catalyst with higher mass specific activity and stability is challenging yet demanding nowadays because of the limited resources available for energy conversion, chemical production, and environmental protection. Among various solid catalysts, supported metal catalysts are most widely studied because of their high activity and/or selectivity for a large amount of important chemical reactions. In such a system, the size and structure of the catalytically active metal particles is always one important factor that determines the performance of a catalyst.^{1–5} Recent studies demonstrated that clusters with diameters less than one nanometer exhibit superiority in catalytic performance compared to common particles with nanometer size.^{2,6–9} Because of the reduced size, clusters have a very high ratio of surface-to-bulk atoms that are coordinatively unsaturated and normally function as active sites. Meanwhile, the deposition of clusters on a support material also

allows the investigation of support effect and metal–support interaction, which is very important in many catalytic processes. Considering the high fraction of the atoms locating at the cluster/support interface, metal–support interaction effect is likely to be much more pronounced in cluster catalysts than typical nanoparticle ones, leading to modification of their structural and electronic features. Therefore, developing the fabrication of a cluster catalyst and deepening the understanding of structure–function relations are of significant interest in heterogeneous catalysis.

The initial investigations of cluster catalysts focused on mass-selected ions produced by physical methods,^{10,11} which provided fundamental insights into the reaction mechanisms

Received: February 1, 2016

Revised: April 4, 2016

of some reactions with clusters.^{12–14} Although the deposition of mass-selected clusters on a support matrix (clusters soft landed on oxide supports) pushes the cluster catalysis from fundamental gas-phase investigations to the conventional field of heterogeneous catalysis, such a fabrication of mass selected clusters is not suitable for practical applications. A more realistic approach via wet chemical method is to be developed. Some efforts have been made to develop the synthesis of subnanometer clusters,^{2,15} even single-atom^{16,17} catalysts in some systems for practical catalysis investigations. However, most of the current systems of cluster or single-atom catalysts are focused on noble metals,^{2,15–17} and investigation of inexpensive and resource-rich transition metal cluster catalysts is rare.^{18,19} Considering that transition metal catalysts have wide and important applications in chemical industry, fabrication of transition metal cluster catalysts, as well as the corresponding structural characterizations and catalytic property studies are of great significance.

In this work, we have applied a facile coprecipitation method with the aid of hydrothermal treatment to prepare subnanometer iron oxide clusters supported on ceria nanorods and nanopolyhedra. Here, the Fischer–Tropsch synthesis (FTS) is chosen as a model reaction to track the relationship between catalytic performance and cluster structure. Unlike the previous assignments on the important active species of iron carbides (Fe_xC_y , such as $\chi\text{-Fe}_3\text{C}_2$,^{20–22} $\epsilon\text{-Fe}_2\text{C}$,^{22,23} etc.), we have found that the subnanometer clusters of iron oxide are stable and catalytically active for FTS reaction. Furthermore, it is demonstrated that finely dispersed iron oxide clusters with Fe–O–Fe coordination structure which dominates in ceria nanorods (NR) are identified as active sites for FTS. On the other hand, the iron oxide clusters formed with strong interaction between Fe atom and CeO_2 support (Fe–O–Ce) in ceria nanopolyhedra (NP) are less active for FTS. The synthesis and structure–function relationship investigation on subnanometer iron oxide clusters provides an opportunity to build a fundamental understanding of electronic and local coordination structure over active site at the atomic level in cluster catalytic systems, which could lead to significant advances in many areas of heterogeneous catalysis.

2. EXPERIMENTAL SECTION

2.1. Catalyst Preparation. The iron–ceria catalysts were prepared via a coprecipitation method with the aids of hydrothermal technique. In the initial step, 0.4 mol/L total amounts of $\text{Fe}(\text{NO}_3)_3 \cdot 9\text{H}_2\text{O}$ (A.R., Sinopharm Chemical Reagent Factory) and $\text{Ce}(\text{NO}_3)_3 \cdot 6\text{H}_2\text{O}$ (A.R., Sinopharm Chemical Reagent Factory) with Fe/Ce molar ratios of 5/95, 15/85, and 25/75 were dissolved in 5 mL of deionized water and stirred for 2 h at room temperature. A brown slurry formed by mixing the above solution with 35 mL of aqueous NaOH of appropriate concentration ($C_{\text{NaOH}} = 6$ or 0.2 mol/L for nanorod or nanopolyhedron sample, respectively) in a 50 mL Teflon bottle. After stirring for another 30 min, this bottle was sealed in a stainless steel autoclave and held at 100 °C for 24 h. After cooling to room temperature, the as-obtained precipitates were filtered, washed with deionized water several times until neutral pH value. The as-washed powders were dried in vacuum at 60 °C for 24 h and then calcined at 400 °C for 4 h (ramping rate: 2 °C/min). The iron–ceria catalysts were designated as αR and αP , where α is the molar percentage of Fe in total metal ions, for nanorod (NR) and nanopolyhedron (NP) samples, respectively. The pure ceria nanorod and

nanopolyhedron samples were labeled as $\text{CeO}_2\text{-R}$ and $\text{CeO}_2\text{-P}$, respectively.

2.2. Characterization. The bulk Fe concentrations in the fresh iron–ceria samples were determined by inductively coupled plasma atomic emission spectroscopy (ICP-AES) with a PerkinElmer 3300DV emission spectrometer.

Transmission electron microscopy (TEM) was conducted on a Philips Tecnai F20 instrument operating at 200 kV. The aberration-corrected HRTEM images and STEM images with the corresponding electron energy loss spectroscopy (EELS) measurements were performed on JEOL ARM200F microscope equipped with probe-forming spherical-aberration corrector and Gatan image filter (Quantum 965). Elemental mapping results were obtained from the Fe–L_{2,3}, Ce–M_{4,5} and O–K edges.

The ex situ X-ray diffraction (XRD) analysis was performed on a Rigaku D/MAX 2550/PC Diffractometer with Ni filtered Cu K α radiation ($\lambda = 1.5406 \text{ \AA}$) operated at 40 kV and 40 mA with a scan step of 0.02°. The in situ XRD patterns were obtained from the same diffractometer by using an Anton Parr XRK-900 reaction chamber. About 100 mg of replicas were loaded in a ceramic sample holder (10 mm in diameter and 1 mm in depth) and then heated from room temperature to 800 °C (interval: 100 °C) with a ramping rate of 30 °C/min in 5% H₂/Ar (30 mL·min⁻¹). At each temperature, two scans (20 min per scan) were measured to obtain the XRD patterns, among which the XRD pattern collecting from the second scan was used for the analysis of crystallinity.

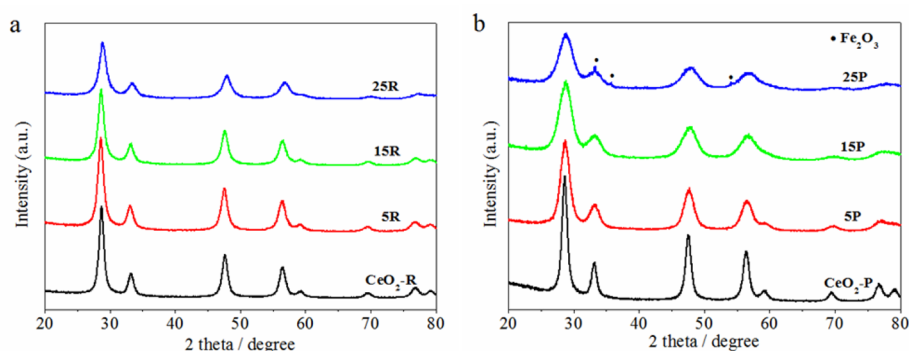
The ex situ X-ray absorption fine structure (XAFS) spectra of Fe K-edge ($E_0 = 7112 \text{ eV}$) for fresh and used iron–ceria samples were collected at BL14W1 beamline of Shanghai Synchrotron Radiation Facility (SSRF) operated at 3.5 GeV under “top-up” mode with a constant current of 220 mA, or at 20-ID-B beamline of Advanced Photon Source (APS) of Argonne National Laboratory (ANL) operated at 7.0 GeV under “top-up” mode with a constant current of 100 mA. The XAFS data were collected under fluorescence mode with a Lytle ion chamber or a 4-channel Vortex silicon drift detector. The energy was calibrated according to the absorption edge of pure Fe foil. Athena and Artemis codes were used to extract the data and fit the profiles.^{24,25} For the X-ray absorption near edge structure (XANES) part, the experimental absorption coefficients as a function of energies $\mu(E)$ were processed by background subtraction and normalization procedures, and reported as “normalized absorption”. On the basis of the normalized XANES profiles, the molar fraction of $\text{Fe}^{3+}/\text{Fe}^{2+}/\text{Fe}^0$ can be determined by the linear combination fit, similar to previous approaches.^{26,27} For the extended X-ray absorption fine structure (EXAFS) part, the Fourier transformed (FT) data in R space were analyzed by applying first-shell approximation or metallic Fe model for the Fe–O/Fe–O–Fe/Fe–O–Ce or Fe–Fe shell, respectively. The passive electron factors, S_0^2 , were determined by fitting the experimental Fe foil data and fixing the Fe–Fe coordination number (CN) to be 8 + 6, and then fixed for further analysis of the measured samples. The parameters describing the electronic properties (e.g., correction to the photoelectron energy origin, E_0) and local structure environment including CN, bond distance (R), and Debye–Waller (D.W.) factor around the absorbing atoms were allowed to vary during the fit process.

X-ray photoelectron spectroscopy (XPS) analysis was performed on an Axis Ultra XPS spectrometer (Kratos, U.K.) with 225 W of Al K α radiation. The C 1s line at 284.8 eV was

Table 1. Fe Concentrations, Surface Ratio of Ce³⁺/Ce⁴⁺, Crystal Phases and Lattice Constants of CeO₂ (*a*), Morphology and Averaged Grain Size (*D*) of Iron–ceria Samples

sample	Fe (at.%) ^a	Ce ³⁺ /Ce ⁴⁺ ^b	phase	<i>a</i> (Å) ^d	<i>D</i> (nm) ^c	morphology
CeO ₂ -R	—	—	fcc CeO ₂	5.3996(9)	10.3	rod
CeO ₂ -P	—	—	fcc CeO ₂	5.4043(2)	9.5	polyhedron
5R	4.8	—	fcc CeO ₂	5.4069(1)	8.4	rod
5P	5.8	—	fcc CeO ₂	5.3908(3)	5.2	polyhedron
15R	15.9	15/85	fcc CeO ₂	5.3984(2)	8.3	rod
		23/77 ^c		5.4070(5) ^c	9.4 ^c	
15P	16.6	15/85	fcc CeO ₂	5.3790(6)	3.7	polyhedron
		23/77 ^c		5.4077(2) ^c	4.5 ^c	
25R	26.5	—	fcc CeO ₂	5.3635(5)	6.8	rod
25P	27.6	—	fcc CeO ₂	5.3697(5)	3.4	polyhedron

^aDetermined by ICP-AES. ^bDetermined by XPS. ^cFor used samples after FTS. ^dCalculated from the XRD patterns by least-squares estimation. ^eCalculated from the XRD patterns by Scherrer equation.

**Figure 1.** XRD patterns of fresh iron–ceria samples: (a) NR; (b) NP.

used to calibrate the binding energies. The fit on specific peaks in each Ce 3d spectrum to obtain the relative ratio of Ce³⁺/Ce⁴⁺ was carried out according to this equation: Ce³⁺/Ce⁴⁺ = $S_{v'}/(S_{v'}+S(v^0, v))$, where $S_{v'}$, $S_{v''}$ and $S(v^0, v)$ stand for the peak area of v' , v'' , and (v^0, v) , respectively.²⁸

The temperature-programmed reduction by hydrogen (H₂-TPR) tests were carried out in a Builder PCSA-1000 instrument (Beijing, China) equipped with a thermal conductivity detector (TCD) to detect H₂ consumption. The fresh catalysts (ca. 30 mg, 20–40 mesh) were pretreated at 350 °C in air for 30 min and then cooled to room temperature in the same atmosphere. After the measured powders were stabilized in pure N₂ at room temperature for about 30 min, they were switched to 10% H₂/Ar and then heated from room temperature to 900 °C with a ramping rate of 5 °C/min.

2.3. Catalytic Tests. The Fischer–Tropsch synthesis (FTS) reaction was conducted on a fixed-bed flow reactor with a gas mixture of 32% CO, 64% H₂, and 4% N₂. Catalyst powders (0.5 g) were diluted with 0.5 g of SiO₂ particles (20–40 mesh) before the test. The FTS measurements at multiple temperatures (230–250 °C) were carried out under a high pressure of 2 MPa with a pretreatment at 350 °C for 3 h in 10% H₂/Ar. The gas hourly space velocity (GHSV) of the reaction was set at 720 cm³ h⁻¹ g_{cat}⁻¹. For the test at fixed temperature, the iron–ceria catalysts were subjected to the same pretreatment and then kept at 2 MPa and 230 °C for 0, 2, 10, or 48 h.

The product and reactant in the gas phase were detected online using a gas chromatograph (GC-9160, Shanghai, China). C₁–C₄ ranged hydrocarbons were analyzed using a Plot Al₂O₃ capillary column with a flame ionization detector (FID);

however, CO, CO₂, CH₄, and N₂ were analyzed by using a Porapak Q and 5A molecular sieve-packed column with a thermal conductivity detector (TCD). To calculate the CO conversion, the 4% N₂ in syngas was used as an internal standard. All hydrocarbons were analyzed using a GC-9160 with a PONA capillary column and a flame ionization detector (FID). The selectivity of the products was based on carbon. For CO₂, the selectivity of which is calculated on the basis of all used CO, whereas the selectivity of CH₄, C₂–C₄, and C₅₊ is calculated on the basis of all hydrocarbons produced.

To minimize the possible reoxidation of used catalysts for structural characterization (XRD, XAFS, XPS and HRTEM-EELS), the iron–ceria samples after FTS were quickly transferred to vials filled with N₂ gas, and the vials were opened just before the additional measurements.

3. RESULTS

3.1. Morphology and Structure of Fresh Iron-Ceria Samples. Table 1 shows that the Fe contents determined by ICP-AES for all the NR and NP samples are in good agreement with those designed, revealing the successful precipitation of both iron and cerium nitrates during synthesis. The XRD patterns in Figure 1 determine a pure fcc fluorite-type CeO₂ (JCPDS card no: 34-394) crystal structure for the fresh iron–ceria samples, except a minor hematite *a*-Fe₂O₃ (JCPDS card no: 33-664) phase for 25P. Table 1 exhibits that the calculated lattice constants (*a*) of CeO₂ varies with Fe concentration. For the NR samples, cell dimension of 5R (5.4069 Å) or 15R (5.3984 Å) is slightly larger than or nearly identical to that of CeO₂-R (5.3996 Å), respectively, although *a* of 25R (5.3635 Å)

is significantly smaller. However, a monotonic decrease in the lattice constants with Fe concentrations appears for NP: $\text{CeO}_2\text{-P}$ (5.4043 Å) > 5P (5.3908 Å) > 15P (5.3790 Å) > 25P (5.3697 Å).

According to Vegard's law, if a Ce^{4+} ion (97 pm, 8-fold coordinated) is substituted by a Fe^{3+} ion (78 pm, 8-fold coordinated) but the adjacent O^{2-} ions (138 pm, 4-fold coordinated) are unchanged, then the calculated cell dimensions for Ce–Fe–O solid solutions are distinctly lower than those measured in XRD, except for a of 5P , which is almost equal to the estimated value, as displayed in Figure 2.

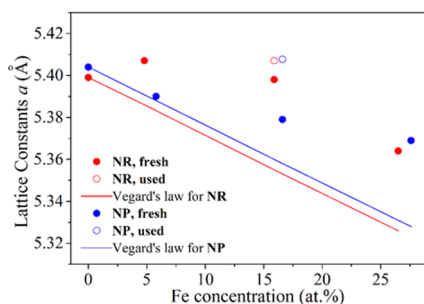


Figure 2. Lattice constants (a) of CeO_2 as a function of Fe concentrations for iron–ceria samples.

Here, the unusual increase of CeO_2 lattice constants for 5R than $\text{CeO}_2\text{-R}$ is due to the size effect,²⁹ which can be verified by its smaller grain size (8.4 nm in Table 1) than that of pure ceria nanorods (10.3 nm in Table 1). The TEM images confirm the shapes of nanorod and nanopolyhedron for different iron–ceria samples. With the increasing Fe concentrations, NR shows more fraction of shorter nanorods (see Figure S1), whereas NP becomes more congregated between nanocrystals (see Figure S2). Thus, according to the XRD and TEM results, we focused on 15R and 15P , which are single-phase with appropriate morphologies (shape and/or aggregation), and selected them as typical NR and NP samples for further investigations on the structure–function relation. The HRTEM and aberration-corrected STEM combining with EELS were performed to obtain the spatial distribution of Fe in the fresh iron–ceria samples at atomic scale (resolution: ~ 1 Å). The HRTEM images in Figure 3a,c exhibit that the nanorods and nanopolyhedra in 15R and 15P were highly crystallized with clear lattice fringes. By the aids of STEM-EELS (see Figure 3b,d and Figure S3), we can see that Ce and O elements were uniformly distributed over the field of view, whereas the Fe-rich microdomains with 0.5–1.2 nm in size were detected for $\text{15R}/\text{15P}$. These microdomains could be originated from the ultrafine iron oxide clusters on the surface of ceria.

The conventional characterizations give the general structural information for the Fe–Ce–O catalysts. However, the specific structure around the measured iron atoms, which is crucial for the identification of the active site, was missing. Therefore, the XAFS technique was used to investigate the iron–ceria samples, which is elementally sensitive and very powerful to determine both electronic and local structures. The XANES region in XAFS responds to the electronic structure of tested metals. The edge energy, the white line intensity, and the pre-edge features are related to the oxidation state of $\text{Fe}^{3+}/\text{Fe}^{2+}/\text{Fe}^0$. Compared to XPS, it takes advantage of milder testing conditions under ambient circumstances. Moreover, the Fe 2P peak is overlapped with the Ce MNN peak in XPS, and the Fe

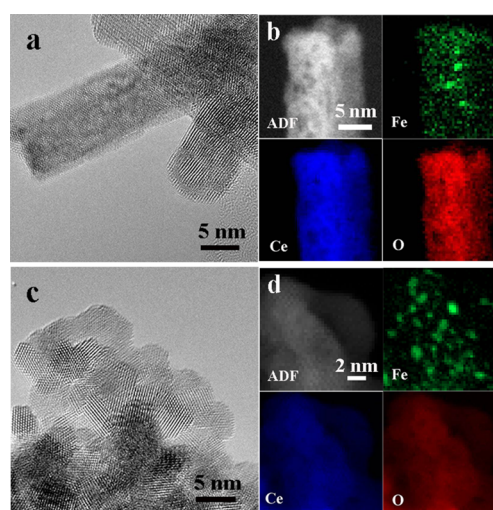


Figure 3. HRTEM images (a,c) and aberration-corrected STEM-EELS results (b,d) of fresh iron–ceria samples: (a,b) 15R ; (c,d) 15P .

3P peak is too weak to provide any reliable information on chemical valence. It can be easily identified from Figure 4a that the pure Fe^{3+} ($\alpha\text{-Fe}_2\text{O}_3$) component, without any fraction of Fe^{2+} (Fe_3O_4) or Fe^0 (Fe foil), appears for 15R and 15P . Thus, we used XANES combined with the linear combination fit to determine the oxidation state of Fe for the iron–ceria samples. The corresponding linear combination fitting results in Table 2 also confirm the fully oxidized Fe^{3+} ions in the fresh samples.

The EXAFS part with the profile fitting in R space was carried out to determine the short-range local structure including distances (R) and coordination number (CN) around the studied iron atoms. From Figure 4b, we can verify a strong peak at 1.96–1.98 Å with a CN of 5.1–5.6 (see Table 2) for the fresh 15R and 15P samples, contributed by the first shell of Fe–O. The fitted R values are different from the Fe–O distances in $\alpha\text{-Fe}_2\text{O}_3$ (1.49 and 2.92 Å) but very close to those of other metal-oxide catalysts such as Au,³⁰ Pt,¹⁵ and Cu.²⁷ Furthermore, the CNs of Fe–O for 15R and 15P are obviously lower than that of Ce–O (CN = 8) in fcc fluorite-type CeO_2 . It indicates that Fe^{3+} ion does not fully replace Ce^{4+} ion and occupy the 8-fold cation site in ceria, which is in good agreement with the XRD results. On the other hand, there is the second coordination shell with much lower intensity than Fe–O for 15R and 15P , which can be assigned to the Fe–M ($M = \text{Fe}$ or Ce) shell in the R space EXAFS spectra (see Figure 4b). We noticed that this can be fitted to a major Fe–Fe path at 2.96 Å with CN of 1.3 and a minor Fe–Ce path at 3.44 Å with CN of 0.6 for 15R and a single Fe–Ce path at 3.50 Å with CN of 1.6 for 15P . Especially, these Fe–Fe and Fe–Ce paths are obviously not the same as the metallic bonds in Fe metal and Fe–Ce bimetals, which have distinctly different R values of 2.46 or 2.84 Å for Fe^0 and 3.09, 3.23, or 3.27 Å for $\text{Ce}_2\text{Fe}_{17}$. The second shells of Fe–Fe are contributed from finely dispersed iron oxide (Fe–O–Fe), and Fe–Ce from the metal–support interaction of Fe–O–Ce, as identified previously for Au–O–Fe³⁰ and Au–O–Ce.³¹

3.2. Catalytic Reactivity of Iron-Ceria Samples for Fischer–Tropsch Synthesis. Figure 5 and Table 3 summarize the catalytic performance of the iron–ceria samples at 230 and 250 °C in FTS after 5 h. 15R exhibits obviously higher CO conversions (22–31%) and activities ($1.0\text{--}1.4 \times 10^{-5} \text{ mol}_{\text{CO}}/\text{g}_{\text{Fe}}/\text{s}$) than 15P ($6.6\text{--}8.4\%$ and $0.3\text{--}0.4 \times 10^{-5}$

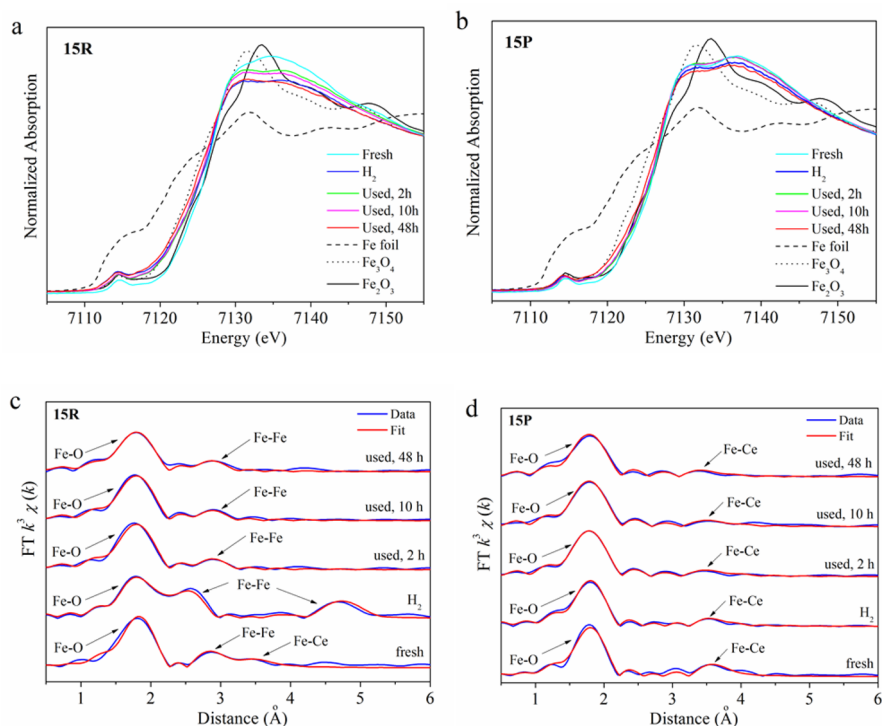


Figure 4. XANES profiles (a,b) and EXAFS spectra in R space (c,d) of the iron–ceria samples at different stages: (a,c) 15R; (b,d) 15P.

Table 2. XANES and EXAFS Results (*R*: Distance; CN: Coordination Number) of Iron–Ceria Samples

sample	δ^a	Fe–O		Fe–Fe		Fe–Ce	
		<i>R</i> (Å)	CN	<i>R</i> (Å)	CN	<i>R</i> (Å)	CN
15R (fresh)	3.0	1.98 ± 0.01	5.6 ± 0.3	2.96 ± 0.04	1.3 ± 0.3	3.44 ± 0.05	0.6 ± 0.6
15R (H ₂)	2.6	1.97 ± 0.01	4.6 ± 0.2	2.50 ± 0.01	1.8 ± 0.3	—	—
				4.12 ± 0.04	0.9 ± 0.6		
				4.84 ± 0.02	5.9 ± 1.4		
15R (used, 2 h)	2.9	1.97 ± 0.01	5.3 ± 0.2	2.98 ± 0.03	0.9 ± 0.3	—	—
15R (used, 10 h)	2.8	1.96 ± 0.01	5.2 ± 0.2	2.97 ± 0.04	0.8 ± 0.3	—	—
15R (used, 48 h)	2.5	1.96 ± 0.01	4.6 ± 0.3	2.97 ± 0.03	0.9 ± 0.3	—	—
15P (fresh)	3.0	1.96 ± 0.01	5.1 ± 0.2	—	—	3.50 ± 0.01	1.6 ± 0.4
15P (H ₂)	3.0	1.95 ± 0.01	4.9 ± 0.2	—	—	3.47 ± 0.02	1.0 ± 0.3
15P (used, 2 h)	3.0	1.96 ± 0.01	5.3 ± 0.2	—	—	3.49 ± 0.03	1.1 ± 0.4
15P (used, 10 h)	3.0	1.96 ± 0.01	5.2 ± 0.2	—	—	3.50 ± 0.03	1.2 ± 0.5
15P (used, 48 h)	2.9	1.95 ± 0.01	4.8 ± 0.2	—	—	3.44 ± 0.03	1.0 ± 0.3

^aDetermined by linear combination analysis on the XANES profiles with the references of bulk Fe foil ($\delta = 0$), Fe₃O₄ ($\delta = 2.67$), and α -Fe₂O₃ ($\delta = 3$).

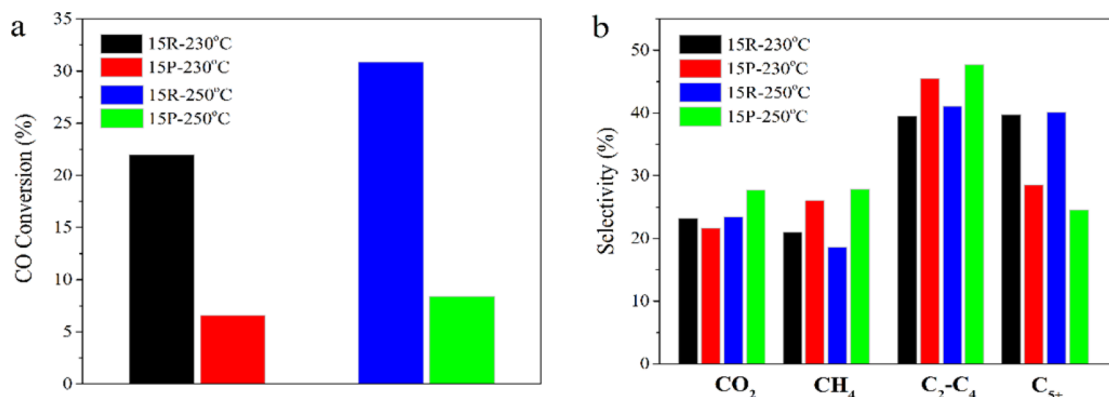


Figure 5. Catalytic reactivity of iron–ceria samples for FTS at 230 and 250 °C: (a) CO conversion; (b) Selectivity of CO₂, CH₄, C₂–C₄ and C₅₊ products. Reaction condition: 0.5 g catalyst, H₂/CO = 2/1, 2.0 MPa, 6 mL·min⁻¹, time on stream of 5 h.

Table 3. Catalytic Reactivity of Iron-Ceria Samples for FTS

sample	T ($^{\circ}\text{C}$)	activity (10^{-5} mol _{CO} /g _{Fe} /s)	CO conversion (%) ^a	CO ₂	selectivity (%) ^b			
					CH ₄	C ₂ –C ₄	C ₅₊	olefin ^c
15R	230	1.0	22	23	21	39	40	56
	250	1.4	31	23	19	41	40	48
15P	230	0.3	6.6	22	26	46	29	61
	250	0.4	8.4	28	28	48	25	53

^aBased on carbon calculations under the following reaction conditions: 0.5 g catalyst, H₂/CO = 2/1, 2.0 MPa, 6 mL·min⁻¹, time on stream of 5 h.

^bBased on carbon calculations for all hydrocarbons (exclude CO₂). ^cOlefin selectivity is calculated by C₂=C₄/C₂–C₄.

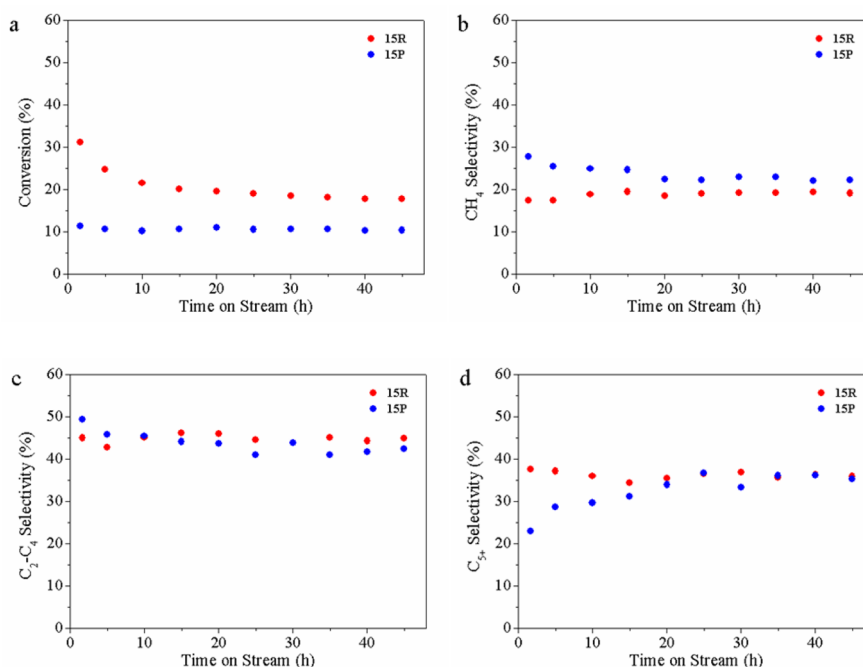


Figure 6. Catalytic reactivity of iron–ceria samples for FTS at 230 $^{\circ}\text{C}$ as a function of time on stream up to 48 h: (a) CO conversion; (b) CH₄ selectivity; (c) C₂–C₄ selectivity; (d) C₅₊ selectivity. Reaction condition: 0.5 g catalyst, H₂/CO = 2/1, 2.0 MPa, 6 mL·min⁻¹.

mol_{CO}/g_{Fe}/s). Furthermore, the selectivity of desired C₅₊ products for 15R (40%) is higher than that of 15P (25–29%), and the selectivity of undesired C₁ products (CO₂ + CH₄) for 15R (42–44%) is slightly lower than that of 15P (48–56%). Fixing the CO conversion of 15R at roughly 10%, which is almost same to that of 15P, even higher selectivity C₅₊ products (53%) was obtained (see Figure S2), further confirming the superiority in catalytic performance for 15R. Additionally, the chain-growth probability (α) obtained from the Anderson–Schulz–Flory (ASF) model³² of 15R was 0.64 (Figure S4), which was higher than that of 15P ($\alpha = 0.57$). In general, all the above results demonstrate that iron on ceria NR is more catalytically active and selective than iron on NP for the FTS reaction. In addition, the as-prepared ceria supported iron oxide clusters (15R) also showed a comparable reactivity with other reported Fe-based catalysts (see Table S1).

Besides that, we also ran the catalytic tests at 230 $^{\circ}\text{C}$ with various reaction times on the iron–ceria samples. Figure 6 presents the overall FTS reactivity for 15R and 15P as a function of reaction time to 48 h. The CO conversion of 15R underwent a rapid drop from 31% to 21% in the initial 10 h and then reached a steady stage with a constant number of ca. 20%; however, for 15P, the CO conversions were almost identical (ca. 10%) throughout the whole test. On the other hand, the changes of selectivity are not significant for the iron–ceria

samples, except for the decrease of CH₄ and increase of C₅₊ for 15P at the beginning of FTS process. Due to the presence of structure–activity relation in heterogeneous catalysis, these differences on catalytic reactivity should be correlated to the related structural evolutions on the active species in Fe–Ce–O system. The fast deactivation of 15R in the initial 10 h during the test is possibly caused by the carbon deposition on the catalyst surface under the high CO conversions.^{33,34} However, the lower CO conversions for 15P result in the lack of deactivation in FTS.

3.3. Morphology and Structure of Used Iron-Ceria Samples. The XRD patterns in Figure S5 exhibit that the crystal structure of fcc fluorite-type CeO₂ was maintained for both 15R and 15P after the transient FTS tests, revealing that no iron-containing phases were generated. Table 1 and Figure 2 identify an increase of ceria lattice constants for the used catalysts (15R: 5.4070 Å; 15P: 5.4077 Å), compared to those for the fresh samples. It reveals that the doped Fe³⁺ ions inside CeO₂ were extracted onto the surface during the H₂-pretreatment and the following FTS process. Meanwhile, it can be seen from Table 1 that there was the crystal growth during the FTS process, and the average grain size of CeO₂ slightly increased from 8.3 nm (15R, fresh) and 3.7 nm (15P, fresh) to 9.4 nm (15R, used) and 4.5 nm (15P, used). The HRTEM images and aberration-corrected STEM-EELS results

in Figure 7, S4 and S5 confirm that ultrafine iron species less than 1 nm were still dominant for the iron–ceria samples after

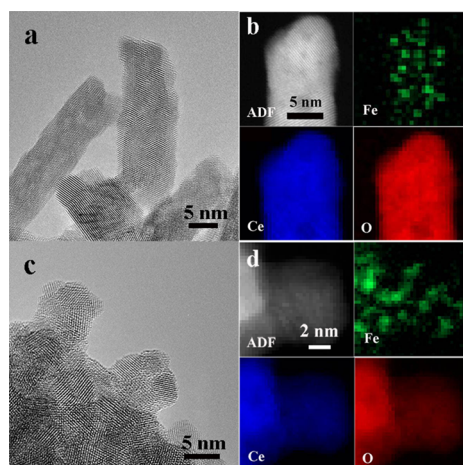


Figure 7. HRTEM images (a,c) and aberration-corrected STEM-EELS results (b,d) of the used iron–ceria samples: (a,b) 15R; (c,d) 15P.

the H_2 -pretreatment (Figure S6), temperature-changing tests (230 and 250 °C, see Figure 7) and temperature-fixed (230 °C, 48 h, see Figure S7) FTS tests. All the above results demonstrate the good stability for 15R and 15P in FTS.

XANES was used to monitor the evolution on electronic structure of $Fe^{\delta+}$ ($\delta = 0-3$) for iron–ceria samples during the long-term stability tests of FTS. The experimental data after different steps of H_2 pretreatment or FTS (2, 10, and 48 h) were obtained by terminating the reaction and measuring the catalyst powders. Figure 4a,b display that no distinct changes for the XANES profiles can be verified for either 15R or 15P in the FTS process. Thus, linear combination fit is required to estimate the averaged oxidation state of iron. Table 2 exhibits that for 15R, the fully oxidized Fe^{3+} ions were reduced to $Fe^{2.6+}$ species (close to Fe_3O_4) in 10% H_2 /Ar at 350 °C for 3 h, consistent with the previous reports on the reducibility of α - Fe_2O_3 .³⁵⁻³⁸ This partially reduced iron was quickly reoxidized to $Fe^{2.9+}$ by 2 h on-stream reaction, possibly due to the oxidation by relatively abundant H_2O and CO_2 in the initial highly active reaction stage. During the sequential FTS process, iron in 15R was gradually reduced and finally transformed to $Fe^{2.5+}$, probably caused by the continuous reduction of syngas under condition of the stable but inferior CO conversion. However, for 15P, all the tested XANES data confirm that the fully oxidized Fe^{3+} species were almost kept the same throughout all the measurements including H_2 pretreatment and FTS reaction (see Table 2).

Figure 4c,d display the EXAFS spectra in R space for the used iron–ceria samples, and the corresponding fitting results are included in Table 2. Besides the first shell of Fe–O at 1.97 Å (CN: 4.6), new Fe–Fe shells at distances of 2.50, 4.12, and 4.84 Å appeared for 15R after the H_2 pretreatment, which are attributed to metallic bonds in Fe metal. It reveals the formation of Fe^0 species in 10% H_2 /Ar, accounting for the decrease of the average iron oxidation state from 3.0 to 2.6 for 15R. However, these Fe–Fe metallic bonds are not present in the EXAFS spectra of H_2 -pretreated 15P (see Figure 4d), and the Fe–O–Ce interaction (Fe–Ce shell at 3.47 Å) was mainly maintained with the lower CN of 1.0 than that of the fresh 15P sample (CN = 1.6).

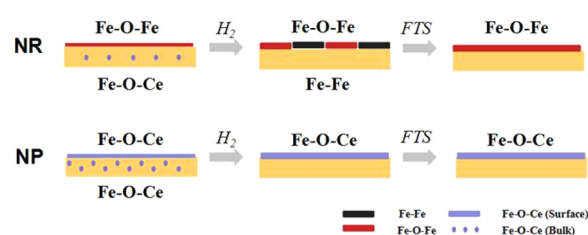
For the iron–ceria samples with different reaction time, their EXAFS spectra exhibit a strong first shell of Fe–O at 1.96–1.97 Å with a CN of 4.6–5.3. However, the profiles of the second shell in the range of 2.5–4 Å show significant differences between 15R and 15P (see Figure 4c,d). After only a 2 h reaction, the metallic Fe–Fe bonds in 15R were totally replaced by the Fe–O–Fe interaction (Fe–Fe shell at 2.98 Å), accompanied by the recovery on the averaged oxidation state of iron from 2.6 to 2.9 (see Table 2). During the sequential reaction until 48 h, the Fe–O–Fe structure was kept the same for 15R (R: 1.95–1.96 Å; CN: 0.8–0.9), but the averaged oxidation state of iron dropped to $Fe^{2.5+}$ at the end of reaction (see Table 2), revealing the formation of Fe^{2+} ions, instead of $Fe^0 + Fe^{3+}$. As for 15P, the second shell was almost identical between H_2 -pretreated and FTS-used for 2, 10, and 48 h (i.e., Fe–Ce at 3.44–3.50 Å with a CN of 1.0–1.2; see Table 2), in good agreement with the constant average oxidation state of Fe^{3+} in XANES.

4. DISCUSSION

4.1. Structural Evolution of Iron on Ceria Nanorods and Nanopolyhedra

Due to the combination between the diverse oxidation states ($Fe^0/Fe^{2+}/Fe^{3+}$ and Ce^{3+}/Ce^{4+}), the complex crystal phases (CeO_2 and α - Fe_2O_3/γ - $Fe_2O_3/Fe_3O_4/FeO/Fe$), the various iron species (single atoms, clusters, and nanocrystals) at atomic–nanometer scales and the different metal–support interactions (strong and weak), it is very difficult to give a full view on the structural evolution of iron on ceria with several limited characterization techniques. Therefore, in this work, multiple advanced instruments, including aberration-corrected STEM-EELS and XAFS (XANES and EXAFS), have been carried out on the typical iron supported on ceria nanoshapes (nanorod and nanopolyhedron). Scheme 1 presents the structural evolution on iron supported on ceria nanorods (15R) and nanopolyhedra (15P).

Scheme 1. Schematic Description of Structural Evolutions on Iron–Ceria Catalysts



First, we need to identify whether the iron species are inside the ceria lattice or on the surface of the oxide support. For the current Fe–Ce–O system, STEM-EELS cannot distinguish between the bulk and the surface of ceria nanorods/nanopolyhedra; EXAFS only works for the local structure around iron atoms; XPS is not useful because of the unavailable Fe 2p spectra (see Figure 8a,b for details). So we estimated the Fe fraction in the CeO_2 lattice by the changes of cell dimensions (see Figure 2 and Table 1) in XRD for different conditions (fresh and FTS-used). Because the a value of 15R (5.4070 Å) or 15P (5.4077 Å) after FTS is higher than or close to that of fresh CeO_2 -R (5.3996 Å) or CeO_2 -P (5.4070 Å), respectively, we assumed that the iron species are totally transferred onto the ceria surface after the reaction, and thus, 0% of Fe is doped into CeO_2 in the used samples. According to

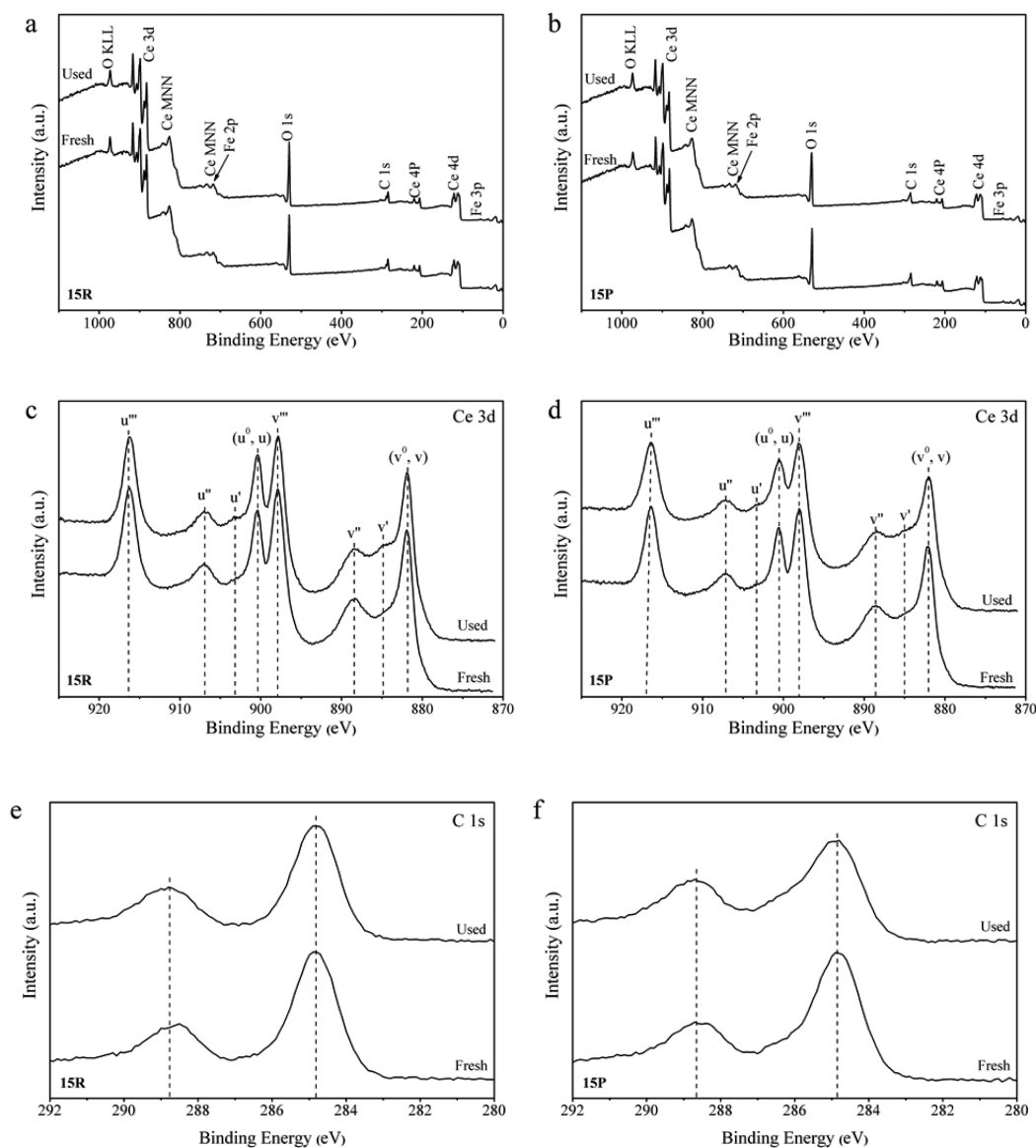


Figure 8. XPS spectra of iron–ceria samples: (a,b) full scale; (c,d) Ce 3d; (e,f) C 1s for **15R** (a,c,e) and **15P** (b,d,f).

the calculation based on Vegard's law, we hypothesized that 100% substitution of Ce^{4+} ion by Fe^{3+} ion leads to the decreased lattice constants of 5.3555 and 5.3558 Å for **15R** and **15P**, respectively. Therefore, the estimated Fe fraction, which is fully doped into ceria, is 17% (**15R**) and 55% (**15P**). It reveals that for the fresh iron–ceria samples, iron species are dominant on the surface of CeO_2 nanorods, whereas nearly half of them are in the core of CeO_2 nanopolyhedra.

Second, we need to identify the local structure of Fe for the iron–ceria catalysts. Although STEM-EELS can provide the direct observations on iron distribution in the Fe–Ce–O system at the atomic scale (~ 1 Å), EXAFS is required to determine the coordinated circumstances of Fe for **15R** and **15P** for the first and/or second shells up to 4 Å. For all the measured samples (fresh, H_2 -pretreated and FTS-used with different reaction time), the strong Fe–O first shell located at ca. 2 Å was determined for both **15R** and **15P** (see Table 2). Thus, the iron structure can be generally described as FeO_x (x is CN of Fe–O), originated from either Fe–O cation–anion bond in doped ceria lattice or ultrafine (< 1 nm) Fe–O clusters on surface of oxide support. The second shell of Fe–Fe at ca. 3

Å in EXAFS can be assigned to Fe– O_x – Fe_y (y is CN of Fe–Fe) structure in FeO_x clusters, whereas the second shell of Fe–Ce at ca. 3.5 Å in EXAFS can be attributed to Fe– O_x – Ce_y (y is CN of Fe–Ce) strong interaction or the chemical bond to FeO_x clusters or inside Fe-doped CeO_2 . Besides, the Fe–Fe metallic bonds with various distances of 2.5, 4.1, and 4.8 Å are determined for the H_2 -pretreated **15R** only. In this work, the origin of two types of iron oxide clusters is the synthetic parameters we applied during the catalyst preparation. High concentration (6 mol/L) of NaOH leads to Fe– O_x – Fe_y , while low concentration (0.2 mol/L) favors Fe– O_x – Ce_y . The morphology of iron–ceria (nanorod and nanopolyhedron) is also governed by the different nucleation and growth processes, due to the concentration of NaOH.

Third, we need to identify the structural evolutions on Fe for the iron–ceria catalysts. Combining the EXAFS analysis with the related XANES linear combination fit, we can deduce the structural evolution of Fe for the iron–ceria catalysts under the different conditions. For all the tested samples, Table 2 reveals that FeO_x (x is about 5) species are the single contribution to the first shell of an iron center, and the average oxidation state

of $\text{Fe}^{\delta+}$ fluctuates from $\text{Fe}^{2.6+}$ to Fe^{3+} . All the above demonstrate that there were no significant transformations on the first shell of iron oxide clusters and FeO_5 structure is very stabilized in Fe–Ce–O system for both **15R** and **15P**, whichever freshly synthesized, H_2 -pretreated, or FTS-used. Considering the contribution by the second shell of Fe–Fe or Fe–Ce in EXAFS, we found that the structural models are not the same for iron supported on different ceria nanoshapes. Specifically, Fe–O₅–Fe_{1.3} (major) and Fe–O₅–Ce_{0.6} (minor) are the iron oxide species for fresh **15R**, although Fe–O₅–Ce_{1.6} is the sole iron structure for fresh **15P**. This is consistent with the related XRD analysis (i.e., more Fe^{3+} ions inside the CeO_2 lattice to form Fe–O–Ce strong interaction for **15P**). Upon H_2 treatment, the iron oxide clusters are converted to FeO_5 plus Fe–Fe_{1.8} metallic bond with the average oxidation state of $\text{Fe}^{2.6+}$ (mixture of Fe^0 and Fe^{3+}) for **15R**. During the sequential FTS process characterized from 2 to 48 h, the above partially reduced iron species are converted to Fe–O₅–Fe, indicating the strong interaction of Fe–O–Fe within the FeO_x clusters. However, for **15P**, the Fe–O₅–Ce species are maintained throughout the whole H_2 pretreatment and FTS reaction. This responds to the strong interaction of Fe–O–Ce in the FeO_x clusters, instead of doped Fe^{3+} ions inside the CeO_2 lattice (XRD results exclude it).

4.2. Modification of Ceria Nanorods and Nanopolyhedra by Iron. As discussed above, we know that the type of ceria support, either nanorod or nanopolyhedron, is directly correlated to the structure of different iron species. On the other hand, the introduction of Fe also modifies the crystal structure of ceria nanoshapes, which has been confirmed by the changes of CeO_2 lattice constants in XRD (refer to section 4.1 and Figure 2). However, FTS happens only on the surface of iron-modified ceria support, and thus, the related surface properties play crucial roles on the catalytic reactivity of Fe–Ce–O. The XPS Ce 3d spectra in Figure 8c,d, together with the peak-deconvolution results in Table 1 show that higher surface $\text{Ce}^{3+}/\text{Ce}^{4+}$ ratios appeared for the used samples (23/77) than the fresh iron–ceria catalysts (15/85) in both **15R** and **15P**. It reveals that the ceria surface was partially reduced after the H_2 pretreatment (350 °C, 10% H_2/Ar) and the sequential FTS process (230–250 °C, 2 MPa, 32%CO/64% H_2/N_2).

In order to further investigate the reducibility of iron supported on different ceria nanoshapes, we applied the H_2 -TPR experiments (Figure 9), accompanied by the in situ XRD

measurements (Figure 10) in 5% H_2/Ar . Figure 9 exhibits that the oxide supports of $\text{CeO}_2\text{-R}$ and $\text{CeO}_2\text{-P}$ have two reduction ranges of 350–550 °C and 650–900 °C, which are attributed to the surface and bulk transformations from Ce^{4+} to Ce^{3+} , respectively.³⁹ However, the $\alpha\text{-Fe}_2\text{O}_3$ reference materials show three peaks centered at ca. 390, 600, and 780 °C for the stepwise reductions of $\alpha\text{-Fe}_2\text{O}_3 \rightarrow \text{Fe}_3\text{O}_4$, $\text{Fe}_3\text{O}_4 \rightarrow \text{FeO}$ (Fe + Fe_3O_4 , disproportionating reaction), and $\text{FeO} \rightarrow \text{Fe}$,^{38,40} respectively. The assignments on different surface oxygen species in H_2 -TPR are very complicated for the iron–ceria samples. In total, there are five and four reduction peaks (A to E in Figure 9) for **15R** and **15P**, respectively. Peak A shows a reduction temperature starting from 220 °C, much lower than that for reduction of surface oxygen in CeO_2 (>350 °C) or transformation of $\alpha\text{-Fe}_2\text{O}_3$ to Fe_3O_4 (>300 °C). This can be assigned to the oxygen species strongly interacting with iron on surface of ceria species, which is due to the weakened Ce–O surface bonds by the addition of Fe. Because a greater fraction of Fe–O–Ce is determined, the starting temperature of peak A for **15P** is lower than that for **15R**. Peak B is very similar to that of $\alpha\text{-Fe}_2\text{O}_3 \rightarrow \text{Fe}_3\text{O}_4$, but the corresponding in situ XRD patterns in Figure 10a,b reveal that no crystallized Fe_3O_4 was generated below 600 °C. Thus, the reduced iron species should be ultrafine FeO_x clusters with the average oxidation state of Fe close to Fe_3O_4 . The end of peak B is around 450 °C, much higher than the temperature of H_2 -pretreatment (350 °C). However, a small fraction of Fe–Fe metallic bond appears for H_2 -pretreated **15R** (EXAFS fitting results in Table 2), indicating that the long-time (3 h) reduction at 350 °C can effectively transfer part of reduced FeO_x cluster into Fe(0) species on the surface of ceria nanorods. Peak C at ca. 500 °C is due to the surface reduction of CeO_2 , which is missing for **15P** because all the surface oxygen species on ceria nanopolyhedra have been activated by the iron addition and reduced at lower temperatures (see peak A). Peaks D and E are located at high temperatures (>550 °C) and not connected to the structural evolutions on the iron–ceria catalysts in FTS: the former can be ascribed to the bulk reduction from Fe_3O_4 to Fe, which was confirmed by the diffraction peaks on the in situ XRD patterns at 600 °C (Figure 10); however, the latter is originated from the reduction of bulk CeO_2 .

From the XRD (lattice constants), EXAFS (fits for Fe–Ce shell), and H_2 -TPR (peaks A and C) results, we can identify that the effect of iron on ceria is correlated to the formation of Fe–O–Ce interaction, which significantly activates the surface oxygen species and shifts their reduction temperature from 450–550 °C down to ca. 220 °C.

4.3. Active Species of Iron-Ceria Catalyst for Fischer–Tropsch Synthesis. In our work, the iron oxide species supported on different ceria nanoshapes (nanorods and nanopolyhedra) show various structural properties, which determine their distinct catalytic performance. So these unique iron–ceria catalysts are good structural models for us to build the structure–activity relation in the Fe–Ce–O system. For the oxide support, the fcc fluorite CeO_2 crystal structure is unchanged, while only the doped iron is transferred from lattice to surface of ceria support during the FTS reaction (see XRD patterns in Figure 1 and S5; cell dimensions in Figure 2 and Table 1). In addition, pure ceria nanoshapes ($\text{CeO}_2\text{-R}$ and $\text{CeO}_2\text{-P}$) did not show any reaction activity (data not given). So, the active sites of iron–ceria catalysts for FTS should be solely related to the Fe-containing phases.

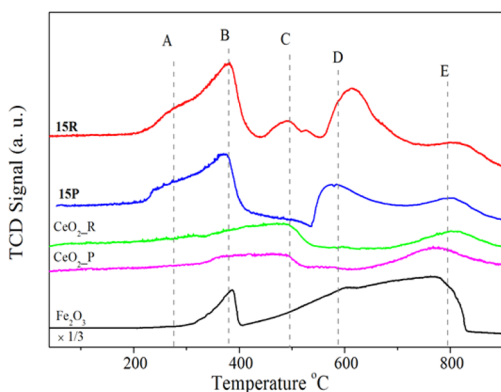


Figure 9. H_2 -TPR profiles of **15R** and **15P** with pure CeO_2 and Fe_2O_3 as referenced materials.

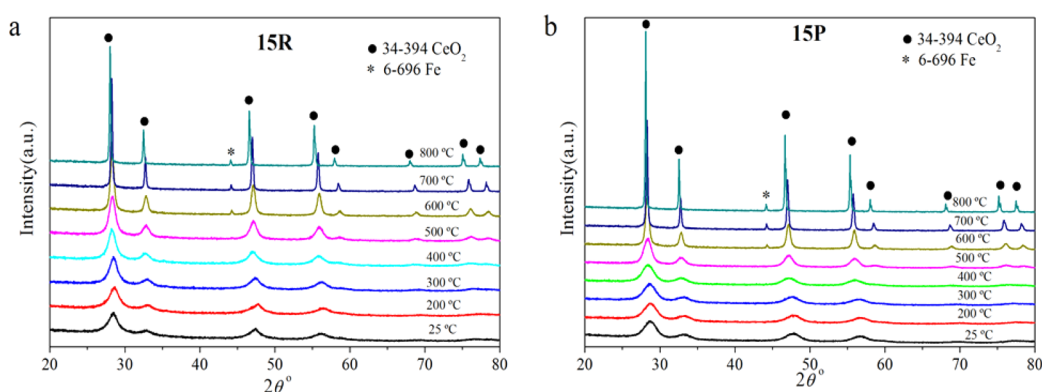


Figure 10. In situ XRD patterns of **15R** (a) and **15P** (b) samples under similar conditions of H_2 -TPR.

Previous findings determined iron carbides (Fe_xC_y such as χ - Fe_5C_2 ,^{20–22} ϵ - Fe_2C ,^{22,23} etc.) originated from iron oxide or metallic iron precursors during the FTS process as the catalytically active phase for Fe-based catalysts. Recent investigations on directly using iron carbides as catalysts for FTS also confirmed this conclusion.^{21,23} However, in our work, we have not detected any iron carbides for subnanometer iron oxide cluster supported on ceria nanoshapes during the different experimental steps (fresh, H_2 -pretreatment, and FTS-reaction). Besides the absence of deeply reduced $Fe^{\delta+}$ ($\delta < 2.5$) species, as confirmed by the XANES analysis, we also identified the carbon species from the C 1s XPS spectra. **Figure 8e,f** show identical profiles between fresh and used samples for both **15R** and **15P** (i.e., the peak at 284.8 eV corresponds to adventitious carbon, and the peak at 288.9 eV is due to the carbonates by the CO_2 adsorption on surface of catalysts).^{41,42} Distinctly, no contributions by carbides can be verified in C 1s XPS spectra. The importance of iron oxide clusters can also be demonstrated by the following discussions.

From **section 3.2**, we can identify that **15R** exhibits higher CO conversion, higher C_{5+} selectivity, and lower CH_4 selectivity than **15P** (see **Figure 5** and **6**, **Table 3**). However, the aberration-corrected STEM-EELS results show very similar Fe-distribution at atomic scale over the fresh, H_2 -pretreated, and used samples for **15R** and **15P** (i.e., FeO_x clusters less than 1 nm). Therefore, the electronic structure and local coordination structure at the atomic level are key factors to govern the reactivity of iron–ceria catalysts in the FTS process.

According to the above discussion, the $Fe^{\delta+}$ ($\delta = 2.6–2.9$) ions in **15R** display better catalytic performance than the Fe^{3+} ions in **15P** (see linear combination fits on XANES in **Table 2**). On the contrary, Ce^{4+} ions were partially reduced to Ce^{3+} ions in FTS, but the ratios of Ce^{3+}/Ce^{4+} are identical between **15R** and **15P** (see XPS results in **Figure 8c,d** and **Table 1**). Thus, the partially reduced iron species contribute more to the FTS reaction than the fully oxidized Fe^{3+} in Fe–Ce–O. The discrepancy on oxidation state is accompanied by different types of metal–support interaction. The FeO_x clusters in **15R** were converted to Fe–Fe metallic bonds in part, while the FeO_x clusters in **15P** were unchanged under the same H_2 pretreatment conditions (see EXAFS fitting results in **Table 2**). The strongly bound Fe–O–Ce structure on ceria activates the surface oxygen species on ceria nanopolyhedra (see H_2 -TPR profiles in **Figure 9**) but does not benefit the FTS reaction. On the other hand, the Fe–O–Fe structure, which weakly interacts with the surface of ceria nanorods, promotes the FTS process.

In summary, we found that partially reduced $Fe^{\delta+}$ ($\delta = 2.6–2.9$) ions in ultrafine (<1 nm) iron oxide clusters, which are in the form of Fe–O–Fe interaction and weakly bound to ceria nanorods, are active species for the FTS reaction. A too strong Fe–O–Ce interaction on ceria nanopolyhedra impairs the reactivity.

5. CONCLUSIONS

In this work, we successfully synthesized subnanometer iron oxide clusters anchored to ceria nanocrystals. The as-synthesized 15 at. % Fe supported on CeO_2 nanorods and nanopolyhedra were used as catalysts in FTS reaction. The results demonstrated that the nanorod sample possesses much higher catalytic activity than the nanopolyhedron one. Insight into the active structure on the iron oxide cluster status in the catalysts for FTS reaction has been provided on the basis of the XANES/EXAFS characterization. By comparing the samples with different reaction time, the conjoint Fe– O_x –Fe_y structure with partially reduced $Fe^{\delta+}$ ($\delta = 2.6–2.9$) species were identified as the precise atomic architecture for the high activity; meanwhile, Fe– O_x –Ce_y clusters with unreduced Fe^{3+} exhibit lower CO conversion and higher selectivity of undesired light hydrocarbons. Generally, this study not only provides a facile method for the synthesis of ultrasmall iron oxide cluster catalysts at subnanometer scale but also reveals that the activity was closely associated with the local coordination structure around the atoms of active site.

■ ASSOCIATED CONTENT

📄 Supporting Information

The Supporting Information is available free of charge on the ACS Publications website at DOI: [10.1021/acscatal.6b00328](https://doi.org/10.1021/acscatal.6b00328).

Comparison on catalytic reactivity, TEM images, XRD patterns of FTS-used samples, HRTEM images and STEM/EELS elemental mapping results of both H_2 -pretreated and FTS-used samples (PDF)

■ AUTHOR INFORMATION

Corresponding Authors

*E-mail: jjacj@sdu.edu.cn.

*E-mail: cma@ustc.edu.cn.

*E-mail: sirui@sinap.ac.cn.

Author Contributions

¶These authors contributed equally (Q.Y. and X.-P.F.).

Notes

The authors declare no competing financial interest.

ACKNOWLEDGMENTS

Financial support has been received from the National Science Foundation of China (NSFC) (grant nos. 21301107, 21373259, 21331001, and 11405256), Fundamental research funding of Shandong University (grant no. 2014JC005), the Taishan Scholar project of Shandong Province (China), and the Hundred Talents project of the Chinese Academy of Sciences, Open Funding from Beijing National Laboratory for Molecular Science, the Strategic Priority Research Program of the Chinese Academy of Sciences (grant no. XDA09030102), the Ministry of Science and Technology (MOST) of China (2014CB932700). Beamline 20-ID-B operations are supported by the U.S. Department of Energy under Contract No. DE-AC02-06CH11357 and the Canadian Light Source.

REFERENCES

- (1) Chen, M.-S.; Goodman, D. W. *Science* **2004**, *306*, 252–255.
- (2) Herzing, A. A.; Kiely, C. J.; Carley, A. F.; Landon, P.; Hutchings, G. J. *Science* **2008**, *321*, 1331–1335.
- (3) Haruta, M. *Catal. Today* **1997**, *36*, 153–166.
- (4) Kang, J.; Zhang, X.; Zhang, Q.; Wang, Y. *Angew. Chem., Int. Ed.* **2009**, *48*, 2565–2568.
- (5) Bezemer, G. L.; Bitter, J. H.; Kuipers, H. P. C. E.; Oosterbeek, H.; Holeywijn, J. E.; Xu, X.; Kapteijn, F.; van Dillen, A. J.; de Jong, K. P. J. *Am. Chem. Soc.* **2006**, *128*, 3956–3964.
- (6) Judai, K.; Abbet, S.; Worz, A. S.; Heiz, U.; Henry, C. R. *J. Am. Chem. Soc.* **2004**, *126*, 2732–2737.
- (7) Turner, M.; Golovko, V. B.; Vaughan, O. P. H.; Abdulkhan, P.; Berenguer-Murcia, A.; Tikhov, M. S.; Johnson, B. F. G.; Lambert, R. M. *Nature* **2008**, *454*, 981–983.
- (8) Vajda, S.; Pellin, M. J.; Greeley, J. P.; Marshall, C. L.; Curtiss, L. A.; Ballentine, G. A.; Elam, J. W.; Catillon-Mucherie, S.; Redfern, P. C.; Mehmood, F.; Zapol, P. *Nat. Mater.* **2009**, *8*, 213–216.
- (9) Lei, Y.; Mehmood, F.; Lee, S.; Greeley, J.; Lee, B.; Seifert, S.; Winans, R. E.; Elam, J. W.; Meyer, R. J.; Redfern, P. C.; Teschner, D.; Schlogl, R.; Pellin, M. J.; Curtiss, L. A.; Vajda, S. *Science* **2010**, *328*, 224–228.
- (10) Lee, S. S.; Fan, C.-Y.; Wu, T.-P.; Anderson, S. L. *J. Am. Chem. Soc.* **2004**, *126*, 5682–5683.
- (11) Yoon, B.; Hakkinen, H.; Landman, U.; Worz, A. S.; Antonietti, J. M.; Abbet, S.; Judai, K.; Heiz, U. *Science* **2005**, *307*, 403–407.
- (12) Feyel, S.; Schroeder, D.; Rozanska, X.; Sauer, J.; Schwarz, H. *Angew. Chem., Int. Ed.* **2006**, *45*, 4677–4681.
- (13) Dong, F.; Heinbuch, S.; Xie, Y.; Rocca, J. J.; Bernstein, E. R.; Wang, Z.-C.; Deng, K.; He, S.-G. *J. Am. Chem. Soc.* **2008**, *130*, 1932–1943.
- (14) Lang, S. M.; Bernhardt, T. M.; Barnett, R. N.; Yoon, B.; Landman, U. *J. Am. Chem. Soc.* **2009**, *131*, 8939–8951.
- (15) Ke, J.; Zhu, W.; Jiang, Y.-Y.; Si, R.; Wang, Y.-J.; Li, S.-C.; Jin, C.-H.; Liu, H.-C.; Song, W.-G.; Yan, C.-H.; Zhang, Y.-W. *ACS Catal.* **2015**, *5*, 5164–5173.
- (16) Qiao, B.-T.; Wang, A.-Q.; Yang, X.-F.; Allard, L. F.; Jiang, Z.; Cui, Y.-T.; Liu, J.-Y.; Li, J.; Zhang, T. *Nat. Chem.* **2011**, *3*, 634–641.
- (17) Yang, M.; Li, S.; Wang, Y.; Herron, J. A.; Xu, Y.; Allard, L. F.; Lee, S.; Huang, J.; Mavrikakis, M.; Flytzani-Stephanopoulos. *Science* **2014**, *346*, 1498–1501.
- (18) Guo, X.-G.; Fang, G.-Z.; Li, G.; Ma, H.; Fan, H.-J.; Yu, L.; Ma, C.; Wu, X.; Deng, D.-H.; Wei, M.-M.; Tan, D.-L.; Si, R.; Zhang, S.; Li, J.-Q.; Sun, L.-T.; Tang, Z.-C.; Pan, X.-L.; Bao, X.-H. *Science* **2014**, *344*, 616–619.
- (19) Lee, S.; Lee, B.; Seifert, S.; Winans, R. E.; Vajda, S. *J. Phys. Chem. C* **2015**, *119*, 11210–11216.
- (20) Yang, C.; Zhao, H.-B.; Hou, Y.-L.; Ma, D. *J. Am. Chem. Soc.* **2012**, *134*, 15814–15821.
- (21) de Smit, E.; Cinquini, F.; Beale, A. M.; Safonova, O. V.; van Beek, W.; Sautet, P.; Weckhuysen, B. M. *J. Am. Chem. Soc.* **2010**, *132*, 14928–14941.
- (22) Mogorosi, R. P.; Fischer, N.; Claeys, M.; van Steen, E. *J. Catal.* **2012**, *289*, 140–150.
- (23) Xu, K.; Sun, B.; Lin, J.; Wen, W.; Pei, Y.; Yan, S.-R.; Qiao, M.-H.; Zhang, X.-X.; Zong, B.-N. *Nat. Commun.* **2014**, *5*, 5783.
- (24) Newville, M. J. *Synchrotron Radiat.* **2001**, *8*, 96–100.
- (25) Ravel, B.; Newville, M. J. *Synchrotron Radiat.* **2005**, *12*, 537–541.
- (26) Frenkel, A. I.; Wang, Q.; Marinkovic, N.; Chen, J.-G.; Barrio, L.; Si, R.; Lopez Camara, A.; Estrella, A. M.; Rodriguez, J. A.; Hanson, J. C. *J. Phys. Chem. C* **2011**, *115*, 17884–17890.
- (27) Wang, W.-W.; Du, P.-P.; Zou, S.-H.; He, H.-Y.; Wang, R.-X.; Jin, Z.; Shi, S.; Huang, Y.-Y.; Si, R.; Song, Q.-S.; Jia, C.-J.; Yan, C.-H. *ACS Catal.* **2015**, *5*, 2088–2099.
- (28) Pfau, A.; Schierbaum, K. D. *Surf. Sci.* **1994**, *321*, 71–80.
- (29) Si, R.; Raitano, J.; Yi, N.; Zhang, L.-H.; Chan, S.-W.; Flytzani-Stephanopoulos, M. *Catal. Today* **2012**, *180*, 68–80.
- (30) Guo, Y.; Gu, D.; Jin, Z.; Du, P.-P.; Si, R.; Tao, J.; Xu, W.-Q.; Huang, Y.-Y.; Senanayake, S.; Song, Q.-S.; Jia, C.-J.; Schüth, F. *Nanoscale* **2015**, *7*, 4920–4928.
- (31) Deng, W.-L.; Frenkel, A. I.; Si, R.; Flytzani-Stephanopoulos, M. *J. Phys. Chem. C* **2008**, *112*, 12834–12840.
- (32) Torres Galvis, H. M.; Bitter, J. H.; Khare, C. B.; Ruitenbeek, M.; Dugulan, A. I.; de Jong, K. P. *Science* **2012**, *335*, 835–838.
- (33) Lohitharn, N.; Goodwin, J. G., Jr.; Lotero, E. *J. Catal.* **2008**, *255*, 104–113.
- (34) Chalupka, K. A.; Maniukiewicz, W.; Mierczynski, P.; Maniecki, T.; Rynkowski, J.; Dzwigaj, S. *Catal. Today* **2015**, *257*, 117–121.
- (35) Zhang, Z.-L.; Han, D.; Wei, S.-J.; Zhang, Y.-X. *J. Catal.* **2010**, *276*, 16–23.
- (36) Perez-Alonso, F. J.; Melián-Cabrera, I.; Granados, M. L.; Kapteijn, F.; Fierro, J. L. G. *J. Catal.* **2006**, *239*, 340–346.
- (37) Jin, Y.-M.; Datye, A. K. *J. Catal.* **2000**, *196*, 8–17.
- (38) Mogorosi, R. P.; Fischer, N.; Claeys, M.; van Steen, E. *J. Catal.* **2012**, *289*, 140–150.
- (39) Fu, Q.; Kudriavtseva, S.; Saltsburg, H.; Flytzani-Stephanopoulos, M. *Chem. Eng. J.* **2003**, *93*, 41–53.
- (40) Hou, W.-J.; Wu, B.-S.; Yang, Y.; Hao, Q.-L.; Tian, L.; Xiang, H.-W.; Li, Y.-W. *Fuel Process. Technol.* **2008**, *89*, 284–291.
- (41) Singh, D.; Soykal, I. I.; Tian, J.; von Deak, D.; King, J.; Miller, J. T.; Ozkan, U. S. *J. Catal.* **2013**, *304*, 100–111.
- (42) Hueso, J. L.; Caballero, A.; Ocana, M.; González-Elipe, A. R. *J. Catal.* **2008**, *257*, 334–344.